Synthesis and electrochemical characterization of Fe and Ni substituted Li$_2$MnO$_3$—An effective means to use Fe for constructing "Co-free" Li$_2$MnO$_3$ based positive electrode material

Mitsuharu Tabuchi [a,*], Yoko Nabeshima [a], Tomonari Takeuchi [a], Hiroyuki Kageyama [a], Kuniaki Tatsumi [a], Junji Akimoto [b], Hideka Shibuya [c], Junichi Imaizumi [c]

[a] National Institute of Advanced Industrial Science and Technology (AIST), 1-8-31 Midorigaoka Ikeda, Osaka 563-8577, Japan
[b] National Institute of Advanced Industrial Science and Technology (AIST), 1-1-1 Higashi, Tsukuba, Ibaraki 305-8565, Japan
[c] Tanaka Chemical Corp., 5-10 Shirakata-cho, Fukui 910-3131, Japan

ABSTRACT

Equal amounts of Fe- and Ni-substituted Li$_2$MnO$_3$ (chemical formula: Li$_{1+x}$[(Fe$_{1/2}$Ni$_{1/2}$)$_y$Mn$_{1-y}$]$_{1-x}$O$_2$, $0 < x < 1/3$, $0.2 \leq y \leq 0.8$) were synthesized using coprecipitation–hydrothermal–calcination. Although the samples with y less than 0.5 are only monoclinic Li$_2$MnO$_3$-type structure ($C2/m$), samples with y larger than 0.6 show a two-phase nature consisting of the monoclinic phase and cubic LiFeO$_2$ phase ($Fm\bar{3}m$). Electrochemical characterization as a positive electrode shows that the Li$_2$O extraction region disappears above $y = 0.6$ on initial charging and that the energy density is decreased drastically above the composition on initial discharging. The optimized transition metal ratios are $y = 0.4$ and 0.5 because the initial average discharge voltage increases with y and the maximum initial cycle efficiency is attained. In the optimized composition, the Fe- and Ni-substituted Li$_2$MnO$_3$ is a 3.5 V class positive electrode, with similar charge and discharge profiles to those of the most attractive active material, NMC positive electrode (chemical formula: Li$_{1+x}$[(Co$_{1/2}$Ni$_{1/2}$)$_y$Mn$_{1-y}$]$_{1-x}$O$_2$, $0 < x < 1/3$, $0.2 \leq y \leq 0.8$). Consequently, Fe can be used as an activator in combination with Ni for constructing "Co-free" Li$_2$MnO$_3$-based positive electrodes. The calcination-condition-dependence of electrochemical properties at the optimized composition is also examined. The effects of the Fe valence state on initial charge–discharge curves are discussed.

© 2010 Elsevier B.V. All rights reserved.

1. Introduction

Lithium-ion batteries (LIBs) are extremely attractive energy storage devices not only for use in cellular telephones and laptop computers but also in electronic vehicles (EVs) and plug-in hybrid vehicle (PHEV) applications. Among the LIB constituent materials, selection of positive electrode materials is the most important because Li-free carbon negative electrodes are used for LIB and the Li ion must be supplied solely from a positive electrode material. Consequently, lithium transition metal oxides such as LiCoO$_2$, LiNiO$_2$, and LiMn$_2$O$_4$ have been selected for practical use because oxidation and reduction of transition metal ion are necessary for Li extraction (charging) and insertion (discharging) processes, respectively [1] at around 3–4 V. The specific capacity values of the materials are 100–180 mAh g^{-1}, which is much less than their ideal capacity of greater than 250 mAh g^{-1}. The fill ratio of positive electrode material and the electrochemically exploitable

amount of Li per the positive electrode material ultimately govern the cell capacity. The adoption of a new positive electrode material with high specific capacity (>200 mAh g^{-1}) is therefore an effective means to increase the LIB capacity and energy density.

Among the proposed new positive electrode materials, Li$_2$MnO$_3$-based positive electrode materials (Li$_{1+x}$(M$_y$Mn$_{1-y}$)$_{1-x}$O$_2$, M = Cr [2], Fe [3], Co [4,5] or Ni [6], $0 < x < 1/3$, $0 < y < 1$) have attracted considerable attention in recent years because of their high specific capacity greater than 200 mAh g^{-1} by taking advantage of an electrochemically inactive Li-rich manganese oxide: Li$_2$MnO$_3$ (ideal capacity: 459 mAh g^{-1}). The appearance of the high specific capacity is explained by regarding them as a yLiMO$_2$–(1 − y)Li$_2$MnO$_3$ (M = Ni$_{1/2}$Mn$_{1/2}$ [7,8] or Ni$_{1/3}$Mn$_{1/3}$Co$_{1/3}$ [9]) composite as follows. On initial charging, Li extraction occurs at less than 4.4 V from the LiMO$_2$ component by oxidation of Co and/or Ni ions until a tetravalent state is reached [7–9]. After finishing Li extraction, Li$_2$O extraction arises from the Li$_2$MnO$_3$ component around 4.5 V [7–9] by oxide ion oxidation [10]. Consequently, the M ion acts as an activator for appearance of the Li$_2$O extraction from Li$_2$MnO$_3$ during the initial charging process. On discharging, only the Li insertion process

* Corresponding author. Tel.: +81 727 51 9618; fax: +81 727 51 9714.
 E-mail address: m-tabuchi@aist.go.jp (M. Tabuchi).

took place at greater than 3.5 V by reduction of Co and/or Ni ions; further Li insertion occurred at less than 3.5 V by reduction of tetravalent Mn ion [6–9]. Therefore, it can be understood easily that the electrochemical property of Li_2MnO_3-based positive electrode materials ($yLiMO_2$–$(1-y)Li_2MnO_3$) depends on transition metal composition y and type M. Although the specific capacity decreases concomitantly with increasing $LiMO_2$ content y, the average discharge voltage increases concomitantly with increasing y [6–9]. However, controlling the initial charge and discharge curves has remained difficult to date because of the appearance of gas evolution [11,12] and irreversible structural change [11] and formation of the solid–electrolyte interfacial (SEI) layer [13] as a result of side-reaction with liquid electrolytes during initial charging up to high voltage limits greater than 4.5 V.

Our group has focused on the development of a $Li_{1+x}(Fe_yMn_{1-y})_{1-x}O_2$ (Fe-substituted Li_2MnO_3) positive electrode material [3,14–16] lying on the $LiFeO_2$–Li_2MnO_3 solid solution. The material is interesting from the viewpoint of constructing a new material design concept. The end member, $LiFeO_2$ phase, is an almost electrochemically inactive phase, different from other 4 V-class positive electrode materials: $LiNi_{1/2}Mn_{1/2}O_2$ and $LiNi_{1/3}Mn_{1/3}Co_{1/3}O_2$. No Fe^{3+}/Fe^{4+} redox has been reported in the relevant literature; only Fe^{2+}/Fe^{3+} redox voltage was detected between 1.5 and 3 V at nano-sized $LiFeO_2$ samples [17]. However, the Fe^{3+}/Fe^{4+} redox appeared at 4 V by making a solid solution with Li_2MnO_3 [3,14], as inferred from first principles calculation [18] and from previous experimental results for $LiFe_yNi_{1-y}O_2$ [19], meaning that Fe ion is useful as activator, as are Co and Ni ions for leveraging a large amount of Li in Li_2MnO_3.

To examine the potential of Fe-substituted Li_2MnO_3, high-temperature charge and discharge behavior (60 °C) under a wide voltage range (2.0–4.5 V) was checked [15,16]. Results showed that Fe-substituted Li_2MnO_3 is classifiable as a 3 V positive electrode with high capacity greater than 200 mAh g^{-1} when the Fe/(Fe + Mn) ratio is adjusted to 0.3–0.5 [15,16]. Recently, the electrochemical behavior of Fe-substituted Li_2MnO_3 has been checked at different test temperatures between +30 and −20 °C within a voltage range of 1.5–4.8 V [20]. We showed that Fe-substitution for Li_2MnO_3 is effective to reduce the irreversible capacity at first cycle and to suppress the gradual change of charge–discharge curves in shape and capacity, fading with increasing cycle number [20]. We noticed that this material is a non-excludable candidate as an inexpensive positive electrode material [20]. However, the average discharge voltage of Fe-substituted Li_2MnO_3 is still too low to apply the typical voltage range of the Li_2MnO_3-based positive electrodes (2.0–4.8 V).

In this work, equal amounts of Fe and Ni ions substitute for Mn and Li in Li_2MnO_3 (chemical formula: $Li_{1+x}[(Fe_{1/2}Ni_{1/2})_yMn_{1-y}]_{1-x}O_2$, $0 < x < 1/3$, $0.2 \leq y \leq 0.8$) lying on $yLi_{1-\delta}(Fe_{1/2}Ni_{1/2})_{1+\delta}O_2$–$(1-y)Li_2MnO_3$ solid solution ($0 < \delta < 1$) for raising the discharge voltage. The δ value depends mainly on the valence state of Ni ions and the crystal structure of $Li_{1-\delta}(Fe_{1/2}Ni_{1/2})_{1+\delta}O_2$ is changeable between cubic ($0.5 < \delta < 1$) and layered ($\delta = 0$) rock-salt structure depending on the δ. First, the transition metal ratio was optimized; then the calcining condition dependence of electrochemical data was checked at the optimized transition metal ratio for additional improvement of the electrochemical performance of the target material.

2. Experimental

All samples ($Li_{1+x}[(Fe_{1/2}Ni_{1/2})_yMn_{1-y}]_{1-x}O_2$, $0 < x < 1/3$, $0.2 \leq y \leq 0.8$) were synthesized using coprecipitation–hydrothermal–calcination (0.25 mol per batch) [15,16,20]. The transition metal mixing ratio was adjusted by changing the

mixing ratio of water-soluble metal salts (reagent grade, Wako Pure Chemical Inds. Ltd.): $Fe(NO_3)_3 \cdot 9H_2O$, $Ni(NO_3)_2 \cdot 6H_2O$, and $MnCl_2 \cdot 4H_2O$. Although the coprecipitation process was the same as the previous one [15,16,20], the hydrothermal reaction time changed from 8 h to 48 h. Before calcination, the product after hydrothermal treatment was washed with distilled water; then the filtrated product was dispersed in LiOH solution including 0.125 mol of LiOH. The mixture was ground well after drying overnight at 100 °C. Calcination conditions were 700 °C or 750 °C for 20 h in air or nitrogen atmosphere. The final product was obtained by washing the calcined mixture with distilled water after grinding and then separating it from the solution using filtration and drying processes. To examine the effect of the Fe valence state on electrochemical behavior, $Li_{1+x}(Fe_{0.2}Mn_{0.8})_{1-x}O_2$ was prepared for comparison using the same synthetic route.

Sample names are defined by the nominal sum of Fe and Ni contents (y) per total transition metal content and calcination condition. For example, two samples 04Y750A and 04Y700N have respective nominal compositions of "$Li_{1+x}[(Fe_{1/2}Ni_{1/2})_{0.4}Mn_{0.6}]_{1-x}O_2$" calcined at 750 °C in air and 700 °C in N_2 atmosphere.

The samples were characterized using X-ray diffraction (XRD) pattern measurements as well as Li, Fe, and Mn elemental analyses using inductively coupled plasma (ICP) emission spectroscopy and average valence state analysis of transition metals through iodometric titration. For X-ray Rietveld analysis, Si powder (SRM 640c) was used as an external standard for calibrating the diffraction angle. The XRD data were collected between 10° and 125° of the 2θ angles under monochromatized CuKα radiation using an X-ray diffractometer (Rotaflex RU-200B/RINT; Rigaku Corp.). A split pseudo-Voigt profile function was selected for each XRD peak fitting. A computer program, RIETAN-2000 [21], was used for X-ray Rietveld analysis.

The particle shape and size were checked using scanning electron microscopy (SEM, JSM-6390; JEOL) with a LaB$_6$ filament. The Brunauer–Emmett–Teller (BET) surface area was measured and used as specific surface area (SSA) data. The particle size distribution was collected for 0.5–350 μm (Aerotrac SPR, 7340; Nikkiso Co. Ltd.). The validity of the obtained particle size distribution was checked using a standard powder (GBM-20; The Association of Powder Process Industry & Engineering, Japan) with average particle size of 22 ± 1.0 μm.

The valence state analysis of Mn or Ni ions was conducted using corresponding metal K-edge X-ray absorption near edge structure (XANES) measurements. These spectra were obtained in transmission mode using a laboratory-type X-ray spectrometer (EXAC-820; Technos Co. Ltd.) at 293 K. As reference samples, $LiMnO_2$ (orthorhombic form), Li_2MnO_3, and NiO and $LiNiO_2$ were used. The ^{57}Fe Mössbauer spectra were recorded at room temperature (Model 222B; Topologic Systems); α-Fe was used for velocity calibration. Observed spectra were fitted to peaks with a Lorenzian line shape. In addition, $LiNi_{0.8}Fe_{0.2}O_2$ were used for comparison.

A coin-type lithium half-cell was used to examine cell properties. A positive electrode was made from a mixture of 5 mg of active material, 5 mg of acetylene black, and 0.5 mg of polytetrafluoroethylene (PTFE) powder. Aluminum mesh was selected as the current collector; Li metal was used as a negative electrode. A typical organic electrolyte – LiPF$_6$/ethylene carbonate (EC) and dimethyl carbonate (DMC, 1:1) – was selected for cell tests. Cell tests started from charging greater than 4.8 V under a fixed current density per unit of mass of the active material, 40 mA g^{-1}; then discharged to 2.0 V at the same current density, unless otherwise specified. Most cell tests were performed at 30 °C. Only on initial charge runs were charging conditions different; a cell was charged up to 5.0 V with 40 mA g^{-1} of current density and then the voltage was fixed under decreasing current density to 10 mA g^{-1} (constant

Table 1
Elemental and average oxidation state of transition metal ions (valence) analyses data, and B.E.T. specific surface area (SSA) and average particle size distribution (D_{50}) values for the $Li_{1+x}[(Fe_{1/2}Ni_{1/2})_yMn_{1-y}]_{1-x}O_2$ samples with various $Fe_{1/2}Ni_{1/2}$ contents. Sample names are defined as the nominal sum of Fe (m) and Ni (n) contents ($m + n = y$) per total transition metal content and calcination condition. For example, two samples 04Y750A and 04Y700N, respectively, have nominal compositions "$Li_{1+x}[(Fe_{1/2}Ni_{1/2})_{0.4}Mn_{0.6}]_{1-x}O_2$" calcined at 750 °C in air and 700 °C in N_2 atmosphere.

Sample	Nominal y	SSA ($m^2 g^{-1}$)	Valence	D_{50} (μm)	Cation content (wt.%)				Li/(Fe + Ni + Mn)	Li_{1+x} $(Fe_mNi_nMn_{1-m-n})_{1-x}O_2$		
					Li	Fe	Mn	Ni		x	m	n
02Y750A	0.2	8.4	3.92	–	10.3	4.87	36.5	4.94	1.78	0.281	0.104	0.101
03Y750A	0.3	9.9	3.80	–	9.86	7.15	32.6	7.33	1.68	0.254	0.151	0.148
04Y750A	0.4	12.0	3.54	8.2 (4)	9.33	10.2	29.4	10.3	1.51	0.203	0.204	0.196
04Y750N	0.4	19.8	3.43	7.2 (4)	8.82	10.3	29.9	10.4	1.40	0.167	0.204	0.196
04Y700A	0.4	21.4	3.49	8.6 (3)	8.90	10.4	29.1	10.2	1.44	0.180	0.209	0.195
04Y700N	0.4	22.5	3.43	8.1 (1)	8.90	10.5	29.8	10.5	1.41	0.170	0.207	0.197
05Y750A	0.5	11.4	3.43	8.1 (3)	8.82	13.3	25.3	13.9	1.36	0.153	0.255	0.253
05Y750N	0.5	23.6	3.33	7.4 (5)	8.18	13.3	25.8	14.0	1.25	0.111	0.252	0.252
05Y700A	0.5	22.7	3.44	9.0 (7)	8.41	13.2	25.0	13.3	1.32	0.138	0.257	0.247
05Y700N	0.5	24.8	3.34	8.3 (3)	8.28	13.8	25.5	13.6	1.27	0.119	0.262	0.246
06Y750A	0.6	10.0	3.17	–	8.27	16.4	20.5	16.7	1.25	0.111	0.309	0.299
08Y750A	0.8	3.4	2.92	–	7.32	21.5	10.9	23.1	1.08	0.0385	0.394	0.403

current–constant voltage (CC/CV) mode) for electrochemical activation.

The discharge characteristics at 30 °C under high current densities to 2.0 V were evaluated from 40 to 3600 mA g^{-1} after charging up to 4.8 V at 40 mA g^{-1}. On initial charging, the above-described CC/CV mode was selected. One cycle test under fixed current density (40 mA g^{-1}) was added before collecting each discharge datum at the desired current density. The discharge behavior at 0 and −20 °C was collected to 2.0 V at a fixed current density, 40 mA g^{-1} after charging up to 4.8 V at 30 °C. Except for the cell test temperature, an identical testing method to that described above was used for high-rate measurements.

3. Results and discussion

3.1. Changes in sample features and electrochemical properties by increased $Fe_{1/2}Ni_{1/2}$ content

To find an optimized transition metal ratio, the samples were compared with a fixed calcination condition (750 °C for 20 h in air). Fig. 1 shows X-ray diffraction patterns of "750A" sample series (samples 02Y750A–08Y750A series) and Li_2MnO_3. Although all observed XRD peaks in each sample can be indexed only by monoclinic unit cell of Li_2MnO_3 ($C2/m$) [22], some of main XRD peaks can overlap the peak position from the unit cell of cubic rock-salt structure ($Fm\bar{3}m$) as mentioned at the end of introduction part. No other crystalline impurity was detected. Smooth peak shift to lower 2θ angle was observed without peak separation trend with increasing $Fe_{1/2}Ni_{1/2}$ content y, suggesting the formation of homogeneous solid solution. These XRD pattern analyses will be described later in detail.

The elemental analysis data of the sample series list in Table 1 with specific surface area and average valence state of Fe, Ni and Mn ions. Observed Fe and Ni contents (m and n values, respectively) showed close agreement with nominal $y/2$ data, indicating that transition metal ratios were controlled accurately by adjusting the mixing ratio of Fe (III) and Ni (II) nitrates and Mn (II) chloride. Li/(Fe + Ni + Mn) ratio, excess amount of Li (x) and average valence state of transition metals decreased concomitantly with increasing Fe and Ni contents, which is a consistent result from increasing $Li_{1-\delta}(Fe_{1/2}Ni_{1/2})_{1+\delta}O_2$ content on $yLi_{1-\delta}(Fe_{1/2}Ni_{1/2})_{1+\delta}O_2$–$(1 - y)Li_2MnO_3$ solid solution ($0 < \delta < 1$). Further valence state analysis for each transition metal will be described in the next section. In summary, chemical analysis and XRD results indicate synthesis of the desired material: $Li_{1+x}[(Fe_{1/2}Ni_{1/2})_yMn_{1-y}]_{1-x}O_2$, $0 < x < 1/3$, $0.2 \leq y \leq 0.8$.

Particle size distribution for 04Y750A was shown in Fig. 2(a). The observed particle size distribution was rather wide (0.6–70 μm); the average particle size of agglomerated particles (see Fig. 2(b), secondary particle size: D_{50}) was 8.2 (4) μm, which corresponds to the particle size at 50% in a cumulative distribution. The small particles around 0.1 μm can be detected by SEM observation (Fig. 2 (c)). In (c), the agglomerated particle consisted from small primary particles around 0.1 μm. Therefore, D_{50} value reflects the agglomerated (secondary) particle size distribution. The secondary particle size was compared among samples later because better electrochemical performance was obtained for Ni substituted Li_2MnO_3 with small particle size as a result of the quite slow Li_2O extraction process around 4.5 V during the initial charge run [23]. To compare the average value of primary size distribution, we use the
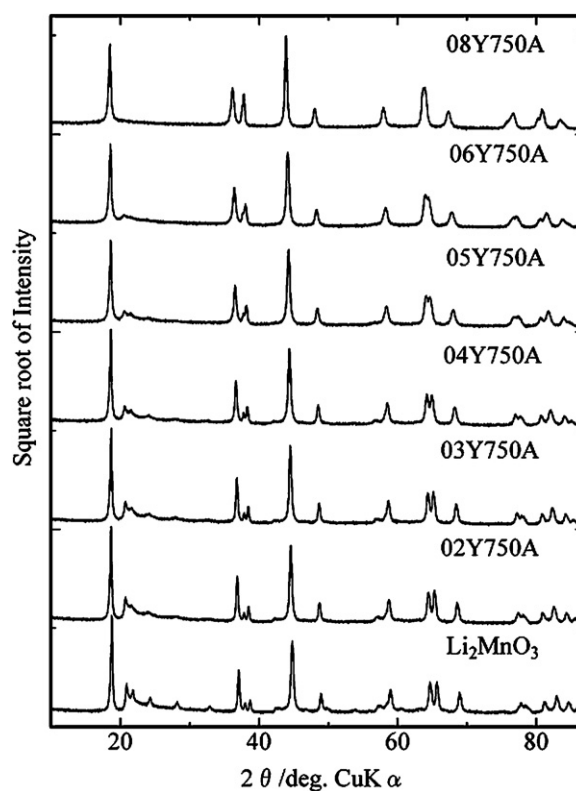
Fig. 1. X-ray diffraction pattern for $Li_{1+x}[(Fe_{1/2}Ni_{1/2})_yMn_{1-y}]_{1-x}O_2$ samples with different $Fe_{1/2}Ni_{1/2}$ contents ($y = 0.2, 0.3, 0.4, 0.5, 0.6$ and 0.8) and Li_2MnO_3. All samples were calcined at 750 °C for 20 h in air atmosphere. See text for sample notation.
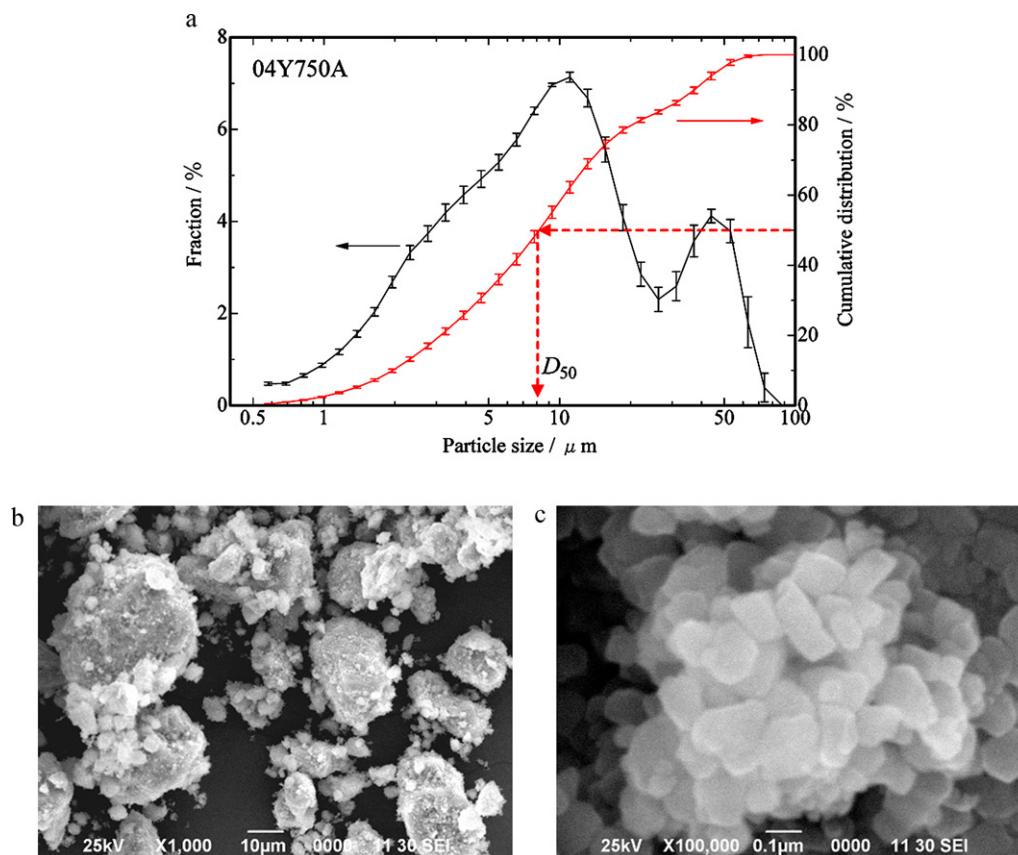
Fig. 2. Particle size distribution (a), and SEM micrographs (b) and (c) for 04Y750A sample. In (a), the average particle size (D_{50}) value corresponds to particle size data at 50% of the cumulative distribution (red line). In (c), right photograph portrays the surface of the agglomerated particles in the left photograph (b).

specific surface area (SSA) values because inverse number of SSA is proportional to the average value of primary size distribution. Monitoring the SSA value is important for interpretation of electrochemical properties of Li_2MnO_3-based positive electrodes because a sample with large SSA value gave large initial discharge capacity [15,16,20,24].

The lattice parameters of observed crystalline phases and their fractions are shown in Table 2a. The sample series from 02Y750A to 05Y750A was a single phase of monoclinic Li_2MnO_3 unit cell ($C2/m$), whereas two samples 06Y750A and 08Y750A contain cubic $LiFeO_2$ phase ($Fm\bar{3}m$) with the monoclinic one as well as Fe-substituted Li_2MnO_3 with higher Fe content greater than 30% [20]. The trend is attributed to the difference in crystal structure of the two end members: Li_2MnO_3 is the monoclinic structure and the crystal structure

of $Li_{1-\delta}(Fe_{1/2}Ni_{1/2})_{1+\delta}O_2$ is changeable between cubic ($0.5 < \delta < 1$) and hexagonal layered ($\delta = 0$) rock-salt structures ($Fm\bar{3}m$ and $R\bar{3}m$, respectively) depending on the δ, which is governed by the valence state of Ni ions. The solubility limit of sum of Fe and Ni ions is into the Li_2MnO_3 structure at $y = 0.5$ ($Li_{1+x}[(Fe_{1/2}Ni_{1/2})_{0.5}Mn_{0.5}]_{1-x}O_2$) under our preparation conditions. The lattice parameters for both unit cells increased concomitantly with increasing $Fe_{1/2}Ni_{1/2}$ content, reflecting that large Fe and Ni ions were substituted for small Mn^{4+} ion, irrespective of these crystalline phases.

The transition metal occupancies (g) are defined, as the occupancy is occupation percentage for each crystallographic site and are presented in Table 2b. Four different cation sites exist for monoclinic Li_2MnO_3 structure, which build up the Li and Li–Mn layers

Table 2a
X-ray Rietveld refinement results for $Li_{1+x}[(Fe_{1/2}Ni_{1/2})_yMn_{1-y}]_{1-x}O_2$ samples with various $Fe_{1/2}Ni_{1/2}$ contents – fractions and lattice parameters of monoclinic and cubic phases.

Sample	Monoclinic ($C2/m$) phase						Cubic ($Fm\bar{3}m$) phase		
	Fraction (%)	a (Å)	b (Å)	c (Å)	β (°)	V (Å^3)	Fraction (%)	a (Å)	V (Å^3)
02Y750A	100	4.9493 (11)	8.5655 (12)	5.0270 (7)	109.066 (17)	201.42 (6)	0	–	–
03Y750A	100	4.9594 (11)	8.5813 (13)	5.0330 (7)	109.263 (16)	202.20 (6)	0	–	–
04Y750A	100	4.9756 (11)	8.6032 (14)	5.0390 (7)	109.243 (18)	203.65 (6)	0	–	–
04Y750N	100	4.9818 (9)	8.6047 (12)	5.0406 (6)	109.253 (15)	203.99 (5)	0	–	–
04Y700A	100	4.9853 (10)	8.5952 (13)	5.0380 (7)	109.233 (15)	203.83 (6)	0	–	–
04Y700N	100	4.9907 (10)	8.6155 (13)	5.0453 (7)	109.201 (17)	204.87 (6)	0	–	–
05Y750A	100	5.0003 (8)	8.6291 (11)	5.0473 (6)	109.250 (13)	205.61 (5)	0	–	–
05Y750N	100	5.0039 (8)	8.6331 (11)	5.0509 (6)	109.238 (12)	206.01 (5)	0	–	–
05Y700A	56	4.999 (3)	8.640 (2)	5.0517 (16)	109.27 (5)	205.95 (14)	44	4.0960 (5)	68.720 (13)
05Y700N	59	5.002 (2)	8.643 (2)	5.0569 (13)	109.33 (3)	206.29 (11)	41	4.1002 (5)	68.932 (13)
06Y750A	78	5.0130 (11)	8.6428 (12)	5.0556 (8)	109.312 (19)	206.71 (6)	22	4.010 (7)	68.97 (2)
08Y750A	48	5.0428 (10)	8.7126 (15)	5.0802 (7)	109.401 (15)	210.53 (6)	52	4.1240 (3)	70.137 (7)

Table 2b

Occupancy (g) of transition metal for each crystallographic site, calculated transition metal contents in the Li layer ($(2g_{4h} + g_{2c})/3$) and the Li–Mn layer ($(2g_{4g} + g_{2b})/3$) and transition metal content per chemical formula ($1 − x$) for monoclinic and cubic phases.

| Sample | Monoclinic (C2/m) phase | | | | | | | Cubic (Fm$\bar{3}$m) phase | |
| | Transition metals in a Li layer | | | Transition metals in a Li–Mn layer | | | $(1 − x)$ in Li$_{1+x}$TM$_{1−x}$O$_2$ | g_{4a} | $(1 − x)$ in Li$_{1+x}$TM$_{1−x}$O$_2$ |
	g_{2c}	g_{4h}	$(2g_{4h} + g_{2c})/3$	g_{4g}	g_{2b}	$(2g_{4g} + g_{2b})/3$			
02Y750A	0	0.053 (4)	0.035 (3)	0.747 (6)	0.491 (7)	0.662 (6)	0.697 (9)	–	–
03Y750A	0	0.051 (4)	0.034 (3)	0.775 (6)	0.507 (6)	0.687 (6)	0.721 (9)	–	–
04Y750A	0	0.062 (3)	0.041 (2)	0.786 (5)	0.550 (5)	0.707 (5)	0.748 (7)	–	–
04Y750N	0	0.075 (3)	0.050 (2)	0.792 (5)	0.588 (5)	0.724 (5)	0.774 (7)	–	–
04Y700A	0.053 (7)	0.048 (5)	0.050 (6)	0.756 (6)	0.568 (6)	0.693 (6)	0.743 (12)	–	–
04Y700N	0.049 (7)	0.055 (5)	0.053 (6)	0.788 (6)	0.597 (7)	0.724 (6)	0.777 (12)	–	–
05Y750A	0.072 (6)	0.045 (4)	0.054 (5)	0.785 (5)	0.599 (7)	0.723 (6)	0.777 (11)	–	–
05Y750N	0.052 (7)	0.097 (5)	0.082 (6)	0.794 (6)	0.654 (6)	0.747 (6)	0.829 (12)	–	–
05Y700A	0	0.032 (11)	0.021 (7)	0.89 (2)	0.68 (2)	0.82 (2)	0.84 (3)	0.387 (8)	0.774 (16)
05Y700N	0	0.032 (10)	0.021 (7)	0.882 (18)	0.710 (18)	0.825 (18)	0.85 (3)	0.395 (9)	0.790 (18)
06Y750A	0.043 (8)	0	0.014 (3)	0.862 (16)	0.672 (14)	0.799 (15)	0.813 (18)	0.402 (18)	0.80 (4)
08Y750A	0	0	0	1	1	1	1	0.429 (4)	0.858 (8)

Imaginary transition metals (TM = Fe$_{y/2}$Ni$_{y/2}$Mn$_{1−y}$) share the same crystallographic site with Li. The sum of the TM and Li occupancies was fixed at unity for all sites. Occupancy of 4h and 2c sites was fixed at zero when negative values were observed after fitting. The transition metal contents per chemical formula ($1 − x$) are calculated as the sum of transition metal contents of two kinds in Li layer ($(2g_{4h} + g_{2c})/3$) and Li–Mn layer ($(2g_{4g} + g_{2b})/3$) for the monoclinic phase, and the ($1 − x$) value correspond to $2g_{4a}$ for the cubic phase.

stacking alternately via the oxide ion layer [22]. Among them, 2c and 4h sites consist of Li layer whereas 4g and 2b sites produce a Li–Mn layer for constructing honeycomb lattice ordering [13]. The 4g sites build up a honeycomb lattice; the 2b site is located on the center of each hexagon. In the series of samples from 02Y750A to 05Y750A, the average amounts of transition metal ion, Fe$_{y/2}$Ni$_{y/2}$Mn$_{1−y}$ occupancy of the Li layer ($(2g_{4h} + g_{2c})/3$) and Li–Mn layer ($(2g_{4g} + g_{2b})/3$) per chemical formula, and their sum ($(1 − x)$) value in Li$_{1+x}$[(Fe$_{1/2}$Ni$_{1/2}$)$_y$Mn$_{1−y}$]$_{1−x}$O$_2$ increased monotonously with increasing Fe$_{1/2}$Ni$_{1/2}$ content, as expected from increasing LiMO$_2$ component on yLiMO$_2$–$(1 − y)$Li$_2$MnO$_3$ solid solution and as expected from the fact that Fe and Ni ions tend to exist on the Li layer of Li$_2$MnO$_3$ [3,13]. These facts indicate that the series of samples from 02Y750A to 05Y750A is considered to be homogeneous solid solution, supporting the conclusion from crystalline-phase constitution and their lattice parameter changes with y value.

Consideration of the difference between g_{4g} and g_{2b} values provides information related to the degree of honeycomb lattice ordering. Ideal honeycomb lattice ordering is accomplished if ($g_{4g} − g_{2b}$) is unity. Complete random fashion is achieved, as in a hexagonal layered rock-salt structure ($R\bar{3}m$), if ($g_{4g} − g_{2b}$) is zero. The difference value was 0.256 (7) for 02Y750A and 0.186 (7) for 05Y750A, indicating greater inhibition of honeycomb lattice ordering occurring concomitantly with an increasing amount of guest cations (Fe and Ni). In fact, the intensity of small peaks between $2\theta = 20°$ and $35°$ reflects honeycomb lattice ordering in the XRD patterns [25]: it decreased concomitantly with increasing guest cation contents.

Although the remainder of the samples, 06Y750A and 08Y750A, contain cubic phase, the ($1 − x$) values for the monoclinic phase were larger than those of 05Y750A, which indicates that substitution of Fe and Ni ions for Mn continued in the monoclinic phase after appearance of cubic phase. The ($g_{4g} − g_{2b}$) values were 0.190 (16) for 06Y750A and 0 for 08Y750A, which means that the monoclinic phase of sample 08Y750A is approximately considered as hexagonal layered rock-salt phase ($R\bar{3}m$). Diminishing the small peaks between $2\theta = 20°$ and $35°$ supports the result described above. In summary, samples 02Y750A–06Y750A have a monoclinic Li$_2$MnO$_3$ type structure with incomplete honeycomb lattice ordering. The ($1 − x$) value of the cubic phase less than 0.9 for 08Y750A, which is lower than the expected value of the end member Li$_{1−\delta}$(Fe$_{1/2}$Ni$_{1/2}$)$_{1+\delta}$O$_2$ ($0 < \delta < 1$, expected ($1 − x$) > 1), suggesting that the cubic phase which contained Mn^{4+} ion originated from Li$_2$MnO$_3$ component (Li$_{4/3}$Mn$_{2/3}$O$_2$, ($1 − x$) = 0.67). Above chemical and XRD analyses and powder properties data were used for understanding the difference in electrochemical data between samples.

Electrochemical data of the "750A" sample series are portrayed in Fig. 3. The obtained electrochemical values are as depicted in Table 3. As described in Section 1, initial charge and discharge curves of yLiMO$_2$–$(1 − y)$Li$_2$MnO$_3$ are divisible into four regions (region A–D) as follows [7,8,10]: Li extraction by oxidation of M ion LiMO$_2$ component (<4.4 V, region A), Li$_2$O extraction by oxidation of oxide ion in Li$_2$MnO$_3$ component (>4.4 V, region B), Li insertion by reduction of oxidized M ion (>3.5 V, region C) and Li insertion by reduction of Mn^{4+} ion (<3.5 V, region D). In initial charging (Fig. 3(a)), the specific capacity at region A increased, although that at region B decreased concomitantly with increasing Fe$_{1/2}$Ni$_{1/2}$ content, as expected. At Li$_{1+x}$[(Fe$_{1/2}$Ni$_{1/2}$)$_{0.6}$Mn$_{0.4}$]$_{1−x}$O$_2$ composition (06Y750A), no region B was detected. Initial discharge curves (Fig. 3(b)) were also changed depending on the Fe$_{1/2}$Ni$_{1/2}$ content. From samples 02Y750A to 05Y750A, the average discharge voltage increased to 3.45 V while maintaining capacity greater than 200 mAh g^{-1}. However, the discharge capacity decreased drastically to less than 170 mAh g^{-1} for 06Y750A and 08Y750A because of the lower contribution of capacity less than 3.5 V (region D) corresponding to the diminished Li$_2$O extraction region (region B).
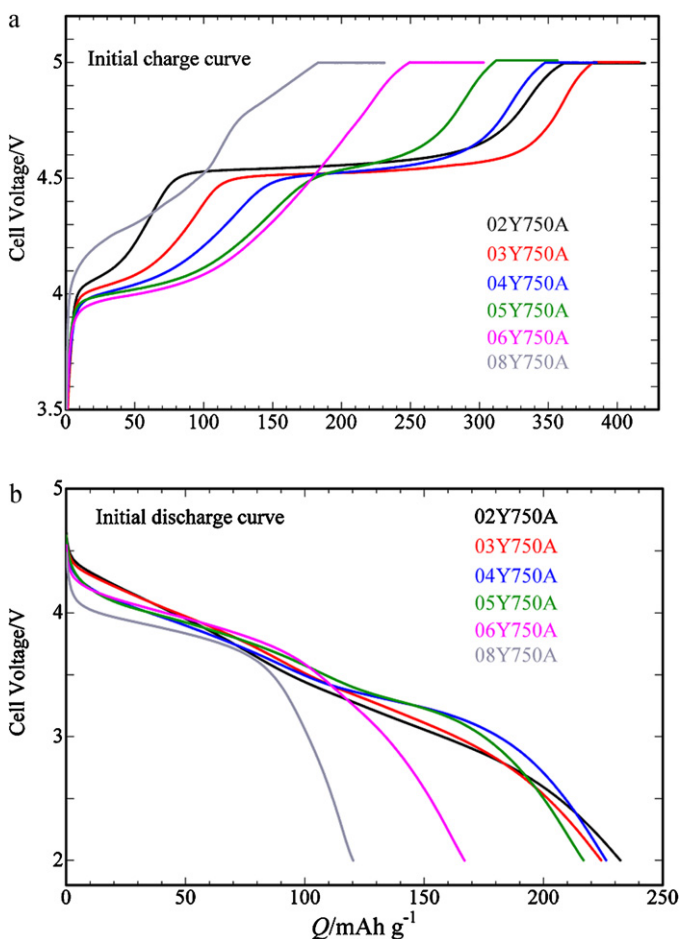
Table 3
Electrochemical charge and discharge characteristics for $Li/Li_{1+x}[(Fe_{1/2}Ni_{1/2})_yMn_{1-y}]_{1-x}O_2$ cells at 30 °C. Data of cells operated between 2.0 and 4.8 V under a fixed current density: 40 mA g^{-1}. Charging remained at the higher upper limit voltage (5.0 V) until reducing the current density to 10 mA g^{-1} only during the initial charging run.

Sample	Q_{1c} (mAh g^{-1})	Q_{1d} (mAh g^{-1})	Q_{1d}/Q_{1c}	V_{ave} (V)	$V_{ave} \cdot Q_{1d}$ (mWh g^{-1})	Q_{20d} (mAh g^{-1})	Q_{20d}/Q_{1d}
02Y750A	420	232	0.553	3.33	774	163	0.703
03Y750A	416	224	0.539	3.39	761	165	0.737
04Y750A	385	226	0.588	3.41	771	171	0.757
04Y750N	349	255	0.731	3.46	884	195	0.765
04Y700A	387	262	0.677	3.39	887	170	0.649
04Y700N	335	232	0.694	3.42	795	166	0.716
05Y750A	357	217	0.608	3.45	747	176	0.811
05Y750N	320	232	0.725	3.51	812	167	0.720
05Y700A	360	232	0.646	3.38	787	166	0.716
05Y700N	355	231	0.652	3.44	797	162	0.701
06Y750A	303	167	0.551	3.54	591	118	0.707
08Y750A	231	120	0.520	3.58	430	38	0.317

Q_{1c}, initial charge capacity; Q_{1d}, initial discharge capacity; Q_{1d}/Q_{1c}, initial efficiency; V_{ave}, average voltage; $V_{ave} \cdot Q_{1d}$, initial discharge energy density; Q_{20d}, 20th discharge capacity.

The trend is similar to the NMC materials, $LiNi_{1/3}Mn_{1/3}Co_{1/3}O_2$–$Li_2MnO_3$ solid solution [9].

To adjust the transition metal ratio, the initial cycle efficiency (Q_{1d}/Q_{1c}), average initial voltage (V_{1d}), and initial discharge energy density ($V_{1d} \cdot Q_{1d}$) data are shown against $Fe_{1/2}Ni_{1/2}$ content (y) as Fig. 4. The high initial cycle efficiency (60%) was obtained at $y = 0.4$ and 0.5. The average initial voltage increased from 3.3 to 3.6 V with increasing y, in contrast to Fe-substituted Li_2MnO_3, whose discharge voltage remained 3.0 V with increasing Fe content [20]. The initial discharge energy density maintained a high value greater than 750 mWh g^{-1} at less than $y = 0.5$. The trends of the three electrochemical parameters engender the conclusion that the optimized transition metal ratio is $y = 0.4$ or 0.5 in the chemical formula $Li_{1+x}[(Fe_{1/2}Ni_{1/2})_yMn_{1-y}]_{1-x}O_2$, which is similar or lower than NMC materials ($y = 0.5$ [26] or 0.7 [9] in $Li_{1+x}[(Co_{1/2}Ni_{1/2})_yMn_{1-y}]_{1-x}O_2$).

The charge and discharge behavior after the 2nd to 20th cycle for all samples (Fig. 5) revealed that the shape change of the curves was suppressed after the cycle proceeding. That behavior contrasts sharply to that of the $LiCoO_2$–Li_2MnO_3 solid solution, whose discharge curves converted slowly to the two sub-plateaus at around 4 V and 3 V with increasing cycle number because of phase transformation to a spinel-like phase [5]. From the viewpoint of the capacity fading up to 20th cycle (Q_{20d}/Q_{1d}), the 05Y750A and 04Y750A samples best accorded with initial charge–discharge behavior.

Fig. 3. Initial charge (a) and discharge (b) curves for $Li/Li_{1+x}[(Fe_{1/2}Ni_{1/2})_yMn_{1-y}]_{1-x}O_2$ sample cells with different $Fe_{1/2}Ni_{1/2}$ contents ($y = 0.2, 0.3, 0.4, 0.5, 0.6$ and 0.8). See text for sample notation.
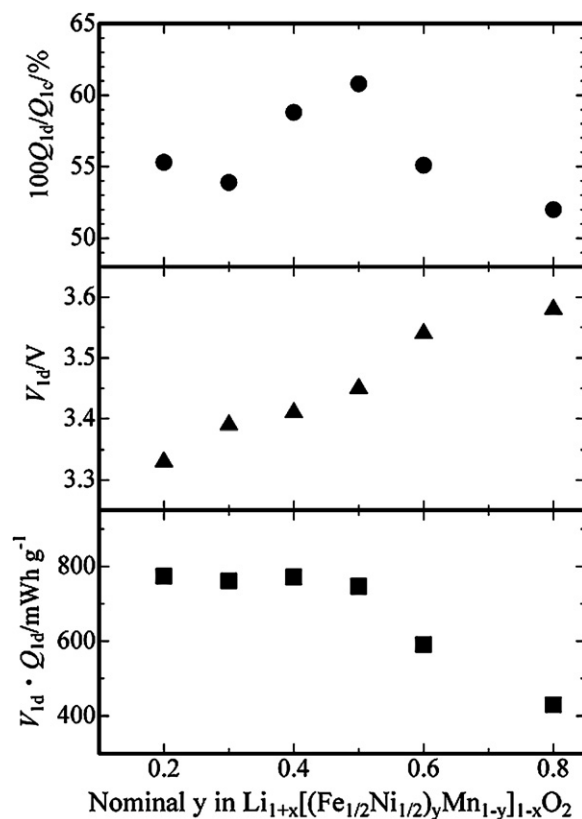
Fig. 4. Plots of initial cycle efficiency (Q_{1d}/Q_{1c}), initial average discharge voltage (V_{1d}) and initial discharge energy density ($V_{1d} \cdot Q_{1d}$) data against nominal $Fe_{1/2}Ni_{1/2}$ content y in $Li_{1+x}[(Fe_{1/2}Ni_{1/2})_yMn_{1-y}]_{1-x}O_2$.
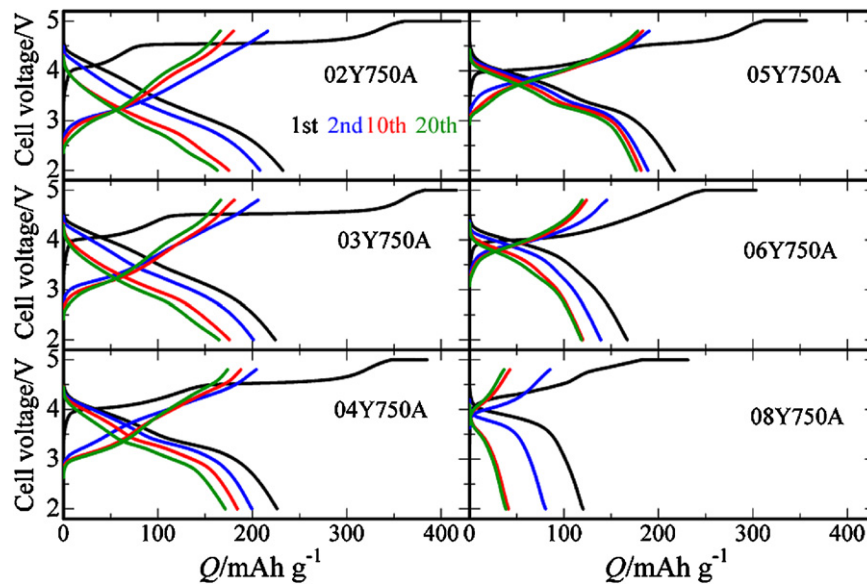
Fig. 5. 1st, 2nd, 10th, and 20th charge and discharge curves for $Li/Li_{1+x}[(Fe_{1/2}Ni_{1/2})_yMn_{1-y}]_{1-x}O_2$ sample cells with different $Fe_{1/2}Ni_{1/2}$ contents ($y = 0.2, 0.3, 0.4, 0.5, 0.6$ and 0.8). See text for sample notation.

The electrochemical performance of the 05Y750A sample was therefore checked up to the 50th cycle (not shown as figure). Almost no shape change in either charge or discharge curves were observed from the 2nd to the end of the cycle test. The discharge capacity after the 50th cycle was 160 mAh g^{-1}, which corresponds to 74% of the initial discharge capacity (217 mAh g^{-1}).

In relation to the chemical composition, Fe and Ni-substitution for Mn is effective to improve the electrochemical property of almost electrochemically inactive Li_2MnO_3 until $y = 0.5$. However, further substitution is ineffective because of the poor electrochemical property of the end member Fe-substituted $LiNiO_2$ [19]. In our solid solution, $y = 0.4$ and 0.5 in $Li_{1+x}[(Fe_{1/2}Ni_{1/2})_yMn_{1-y}]_{1-x}O_2$ are optimized chemical compositions. The observed specific surface area (SSA) values greater than 10 m^2 g^{-1} can contribute to improvement of the initial cycle efficiency at the optimized composition. In fact, the initial cycle efficiency is improved with increasing SSA value for Fe-substituted Li_2MnO_3 [15,16]. Careful phase fraction determination through X-ray Rietveld analysis is important because the samples 06Y750A and 08Y750A coexisting cubic rock-salt phase exhibited poor electrochemical performance. The appearance of cubic rock-salt phase is one of demerit of Fe incorporation in Li_2MnO_3 structure. The synthetic efforts for minimizing the formation of the cubic phase are needed.

3.2. Change in sample features and electrochemical properties by changing calcination conditions at optimized $Fe_{1/2}Ni_{1/2}$ content

To improve the electrochemical performance at optimized transition metal ratios ($y = 0.4$ or 0.5 in $Li_{1+x}[(Fe_{1/2}Ni_{1/2})_yMn_{1-y}]_{1-x}O_2$), several calcination conditions at 700 °C or 750 °C were applied in air or nitrogen atmosphere. Especially, effects of an inert (N_2) atmosphere were examined because transition metals in $LiMO_2$–Li_2MnO_3 positive electrodes were reduced compared to the as-prepared one after the end of the first cycled state; thereby a high reversible capacity was obtained in the subsequent cycles [7,8,10].

No impurity phase was detected in XRD patterns for $y = 0.4$ and 0.5 (see Fig. 6 for $y = 0.4$). Table 1 shows that the samples prepared in N_2 atmosphere had a lower $Li/(Fe+Ni+Mn)$ ratio and average valence state of transition metal cation than those of samples prepared in an air atmosphere at a fixed temperature, which means a decrease in excess amount of Li, x in $Li_{1+x}[(Fe_{1/2}Ni_{1/2})_yMn_{1-y}]_{1-x}O_2$

by reduction of constituent transition metals. The SSA values for the samples prepared in N_2 atmosphere were higher than those for the samples prepared in air atmosphere, especially at 750 °C, which was supported by SEM observation, as depicted in Fig. 7 ($y = 0.4$). As described previously, the SSA value is inversely proportional to the primary particle size; thereby, both samples 04Y750N and 05Y750N consisted of finer grains than those of corresponding samples 04Y750A and 05Y750A, respectively. In the particle size distribution of secondary (agglomerated) particles, samples obtained in the N_2 atmosphere had a higher fraction
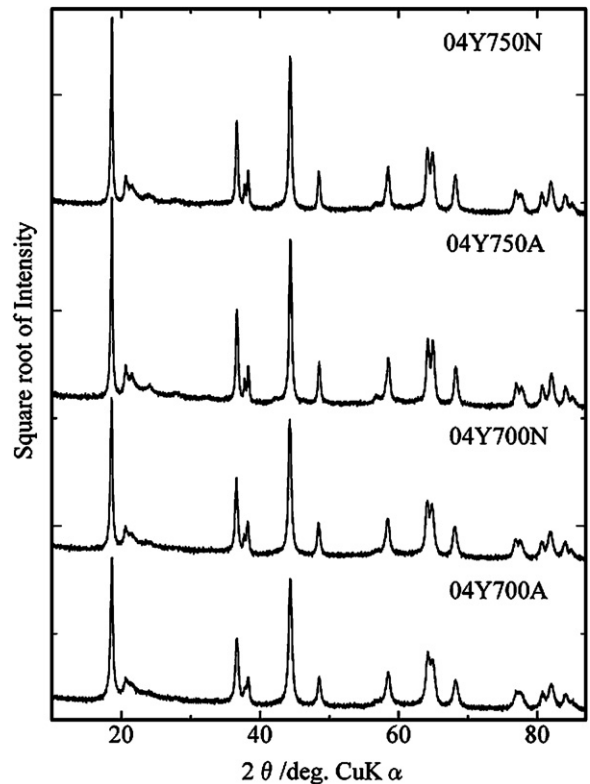
Fig. 6. X-ray diffraction pattern for $Li_{1+x}[(Fe_{1/2}Ni_{1/2})_{0.4}Mn_{0.6}]_{1-x}O_2$ samples with different calcination conditions. See text for sample notation.
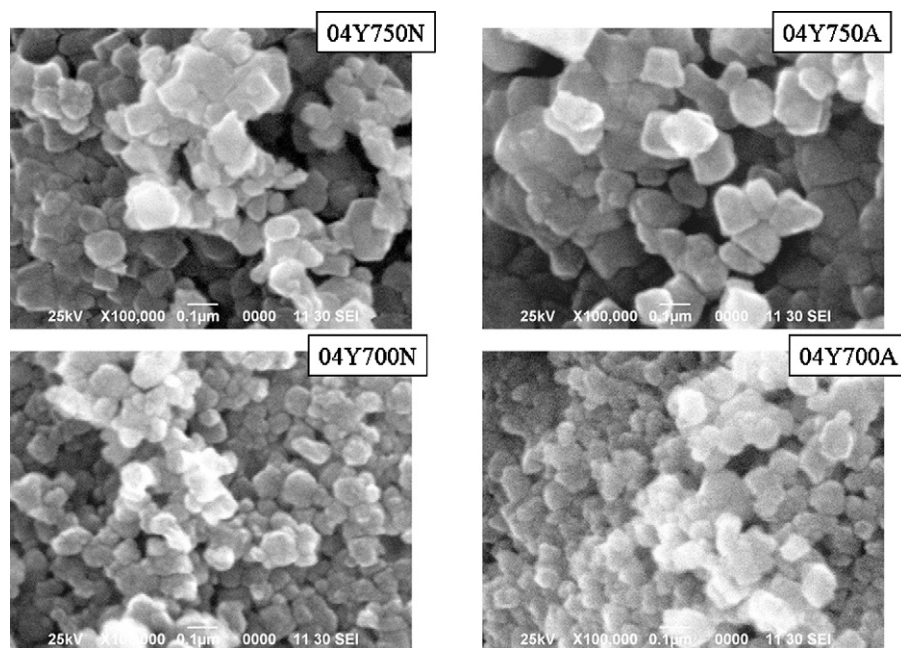
Fig. 7. SEM micrographs for "04Y" sample series ($Li_{1+x}[(Fe_{1/2}Ni_{1/2})_{0.4}Mn_{0.6}]_{1-x}O_2$).

of agglomerated particles less than 10 μm than those of correspondent samples obtained in the air atmosphere. Consequently, slightly smaller average particle size distribution (D_{50}) values were obtained, meaning that the calcination in N_2 atmosphere reduces not only grain growth but also agglomeration of primary particles.

X-ray Rietveld analysis (Table 2a) revealed that the "04Y" samples series maintained a single phase of monoclinic Li_2MnO_3 structure that was independent of the calcination condition. In contrast, in the "05Y" sample series, the samples prepared at 700 °C were two-phase feature of monoclinic Li_2MnO_3 and cubic $Li_{1-\delta}(Fe_{1/2}Ni_{1/2})_{1+\delta}O_2$ phases, although those prepared at 750 °C were a single phase of monoclinic Li_2MnO_3 solid solution. That fact suggests that the observed two-phase coexisting state was a layered–cubic rock-salt composite state, as was the Fe-substituted Li_2MnO_3 [27]. The lattice volume (V) and ($1 - x$) values of the monoclinic and cubic phases for the samples obtained in N_2 atmosphere were invariably higher values than those for correspondent samples obtained in air atmosphere. The trend supports the deduction reached based on results of chemical analyses: the decrease in x value in the chemical formula $Li_{1+x}[(Fe_{1/2}Ni_{1/2})_yMn_{1-y}]_{1-x}O_2$ resulted from reduction of transition metals, as expected by selection of an inert atmosphere.

The calcination temperature and atmosphere dependence of electrochemical data were examined using "04Y" sample series, as presented in Fig. 8 and Table 3. In the initial charge curve, samples 04Y750N and 04Y700N showed smaller specific capacity values at the Li_2O extraction region than those of 04Y750A and 04Y700A. That trend can be anticipated from the decreasing x value in $Li_{1+x}[(Fe_{1/2}Ni_{1/2})_yMn_{1-y}]_{1-x}O_2$ because a previous study [10] demonstrated that the specific capacity for Li_2O extraction part decreased with the excess amount of Li (x) per the chemical formula ($Li[Li_xM_{1-x}]O_2$). It is particularly interesting that the initial cycle efficiency (Q_{1d}/Q_{1c}) is drastically improved from 59% (04Y750A) to 73% (04Y750N) and that the initial discharge capacity and discharge energy density of sample 04Y750N (255 mAh g^{-1} and 884 mWh g^{-1}) were higher than those of 04Y750A (226 mAh g^{-1} and 771 mWh g^{-1}). The result indicates that calcination in a nitrogen atmosphere is an effective means to improve initial electrochemical properties of Li_2MnO_3-based positive electrodes. In contrast, the difference in electrochemical data between samples

04Y700N and 04Y700A is small, as Table 3 shows. From this fact and difference in SSA and D_{50} values among the samples, the above initial cycle efficiency improvement for sample 04Y750N can be attributed to suppression of grain growth and agglomeration by calcination in a N_2 atmosphere. The discharge capacity retention values after the 20th cycle (Q_{20d}/Q_{1d}) for samples 04Y750A and
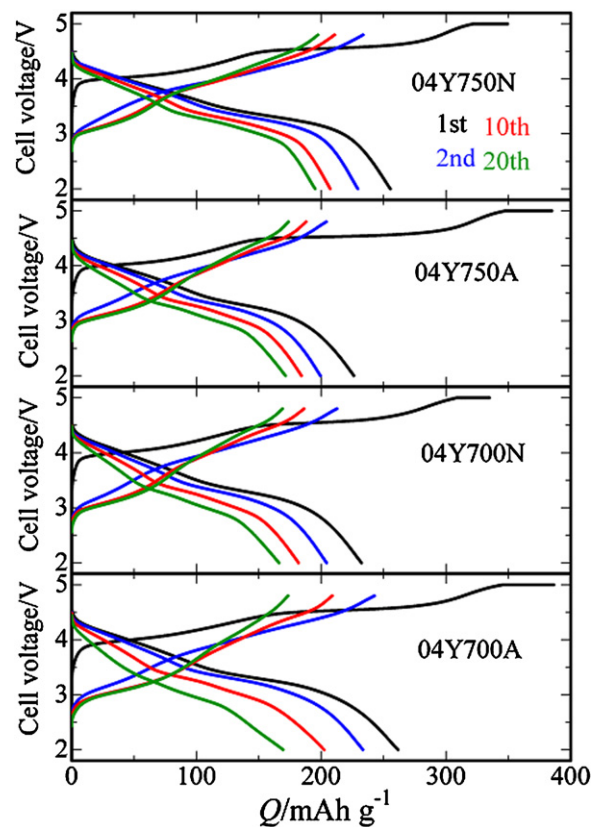

Fig. 8. 1st, 2nd, 10th, and 20th charge and discharge curves for Li/$Li_{1+x}[(Fe_{1/2}Ni_{1/2})_{0.4}Mn_{0.6}]_{1-x}O_2$ sample cells with different calcination conditions.
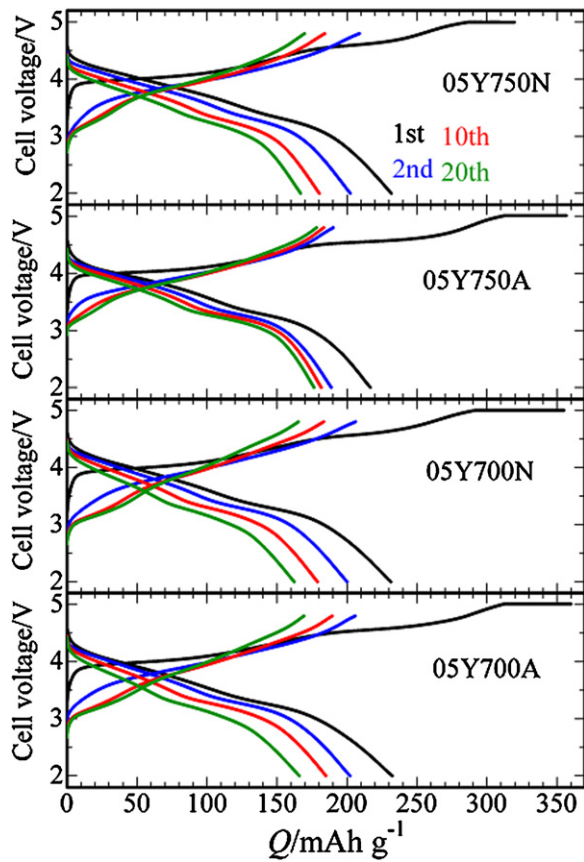
Fig. 9. 1st, 2nd, 10th, and 20th charge and discharge curves for Li/Li$_{1+x}$[(Fe$_{1/2}$Ni$_{1/2}$)$_{0.5}$Mn$_{0.5}$]$_{1-x}$O$_2$ sample cells with different calcination conditions.

Fig. 10. Discharge curves for Li/Li$_{1+x}$[(Fe$_{1/2}$Ni$_{1/2}$)$_y$Mn$_{1-y}$]$_{1-x}$O$_2$ sample cells ($y = 0.4$ or 0.5) under three current densities (40, 600 and 1200 mA g^{-1}) after charging up to 4.8 V.

04Y750N were higher than those for 04Y700A and 04Y700N, indicating that calcination greater than 750 °C is necessary for the present preparation method.

The electrochemical data of the 04Y750N sample were therefore collected until the 50th cycle (not shown as figure). Almost no shape change in either charge or discharge curves was observed from 2nd to the end of cycle test. The discharge capacity after the 50th cycle was 169 mAh g^{-1}, which corresponds to 69% of the initial discharge capacity (244 mAh g^{-1}).

The 1st to 20th charge and discharge curves for the "05Y" sample group are depicted in Fig. 9; the electrochemical parameters are presented in Table 3. The positive effect of calcination in N$_2$ atmosphere on electrochemical data was observed for the 05Y750N sample just as it was for the 04Y750N sample. However, the Q$_{20d}$/Q$_{1d}$ values for the remaining samples except for the 05Y750A sample (81%) was poor, about 70–72%. The reason remains unknown.

Fig. 10 and Table 4 expressed the discharge characteristics under high current density for the "04Y" and "05Y" sample series. The samples obtained by calcination in nitrogen atmosphere (04Y750N and 05Y750N) exhibited better electrochemical performance than those of correspondent samples obtained by calcination in air (04Y750A and 05Y750A) up to 1200 mA g^{-1}. That positive result is attributable to minimizing the decrease in SSA value by calcination in nitrogen atmosphere at 750 °C (see Table 1) because Fe-substituted Li$_2$MnO$_3$ with high SSA value exhibited a better high-rate performance [20]. Consideration based on SSA values

Table 4

Electrochemical discharge characteristics from 4.8 to 2.0 V for Li/Li$_{1+x}$[(Fe$_{1/2}$Ni$_{1/2}$)$_y$Mn$_{1-y}$]$_{1-x}$O$_2$ cells under different current density and temperature at less than 30 °C at a fixed current density. Charging remained at higher upper limit voltage (5.0 V) until reducing the current density to 10 mA g^{-1} only during the initial charging run. The rate performance of cells was taken by discharging them under high current density greater than 40–3600 mA g^{-1} at 30 °C after charging to 4.8 V at 40 mA g^{-1}. The low-temperature property of the cells was taken by discharging them under different temperatures (30, 0 and −20 °C) after charging to 4.8 V at 40 mA/g at 30 °C. After each discharge test, the cell charged and discharged at 40 mA g^{-1} and 30 °C before the next discharge test.

Sample	Discharge capacity under different current density (mAh g^{-1})						Discharge capacity under different temperatures (mAh g^{-1})		
	40 mA g^{-1}	120 mA g^{-1}	600 mA g^{-1}	1200 mA g^{-1}	2400 mA g^{-1}	3600 mA g^{-1}	30 °C	0 °C	−20 °C
04Y750A	216	173	140	101	60	49	229	139	62
04Y750N	266	213	179	149	89	59	234	148	57
04Y700A	234	193	157	130	89	63	263	176	81
04Y700N	248	202	174	140	84	63	243	155	64
05Y750A	212	162	115	88	63	50	214	98	46
05Y750N	229	182	144	107	65	51	239	140	62
05Y700A	215	166	132	107	73	57	228	121	56
05Y700N	219	170	134	106	74	56	228	124	56
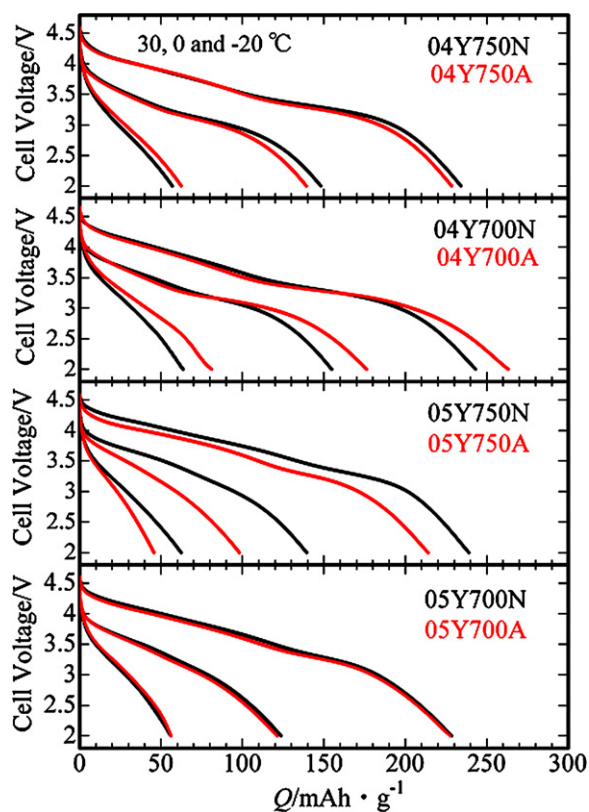
Fig. 11. Discharge curves for $Li/Li_{1+x}[(Fe_{1/2}Ni_{1/2})_yMn_{1-y}]_{1-x}O_2$ sample cells ($y = 0.4$ or 0.5) cells under three temperatures (+30, 0 and $-20\,°C$) after charging up to 4.8 V.

can explain the negligibly small difference in the high-rate performance between samples calcined at 700 °C, whose SSA values were mutually similar.

Low-temperature discharge characteristics are presented in Fig. 11 and Table 4. In contrast to high-rate characteristics, only the 05Y750N sample had better discharge characteristics than 05Y750A, although the 04Y750N sample had almost identical characteristics to those of 04Y750A, in spite of possessing a large SSA value. Further examination is necessary for improvement of low-temperature characteristics.

Above result showed that the electrochemical data of our material is improved by calcination in inert atmosphere. To find the origin, we examine the valence state analysis of each transition metal in the next part.

3.3. Extraction of Fe valence state effect on initial electrochemical properties at optimized $Fe_{1/2}Ni_{1/2}$ contents ($y = 0.4$)

To extract further beneficial information for constructing the material design, Mn and Ni K-edge XANES and ^{57}Fe Mössbauer spectra were taken for the "04Y" sample group. The Mn K-edge XANES spectra (Fig. 12) for all samples overlapped that for Li_2MnO_3, instead of orthorhombic $LiMnO_2$, which indicates the unchanged tetravalent nature of Mn ion. Meanwhile, the Ni K-edge XANES spectra (Fig. 13) mutually differed, although these peak-top positions were situated between NiO (2+ state, 8.345 keV) and $LiNiO_2$ (3+ state, 8.349 keV). Formal Ni valence is calculable using above peak-top energy data of the standard materials and assuming that the energy at peak top position changes linearly with the valence state of Ni ion between 2+ and 3+ states according to the method applied for Fe K-XANES [17].

The Ni valence was calculated as follows: the Ni valence states for samples 04Y750N, 04Y750A, 04Y700N, and 04Y700A were cal-
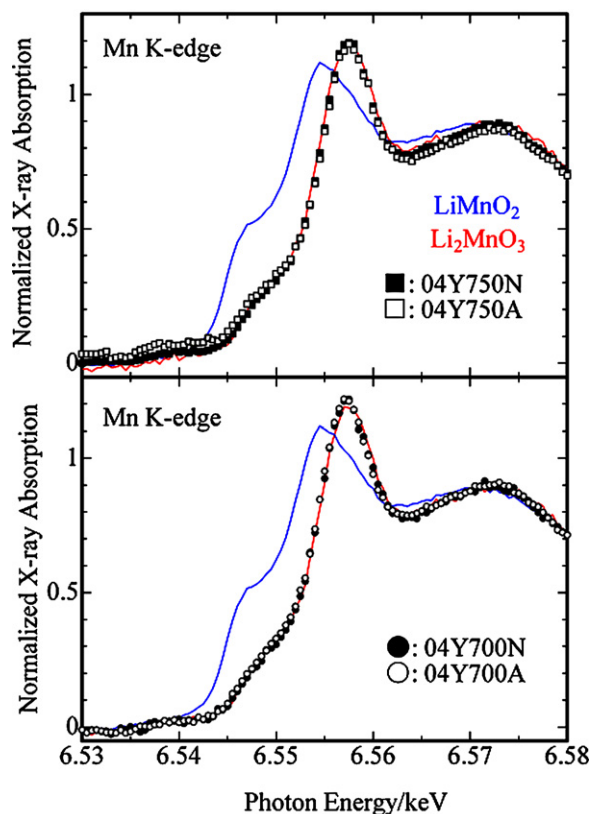

Fig. 12. Mn K-edge XANES spectra for "04Y" sample series ($Li_{1+x}[(Fe_{1/2}Ni_{1/2})_{0.4}Mn_{0.6}]_{1-x}O_2$) with those for standard materials, $LiMnO_2$ and Li_2MnO_3.
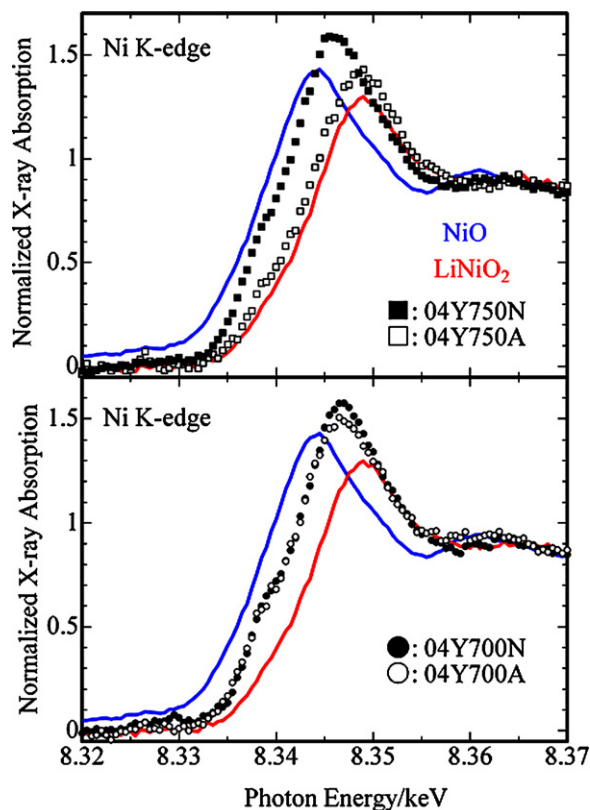
Fig. 13. Ni K-edge XANES spectra for "04Y" sample series ($Li_{1+x}[(Fe_{1/2}Ni_{1/2})_{0.4}Mn_{0.6}]_{1-x}O_2$), with those for standard materials, NiO and $LiNiO_2$.
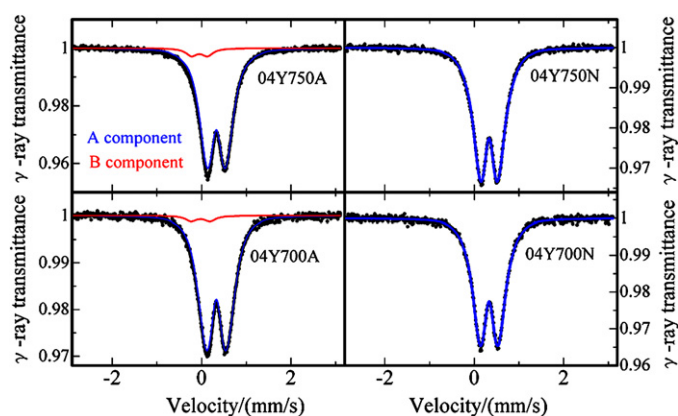
Fig. 14. Observed (closed circle) and calculated (solid curve) ^{57}Fe Mössbauer spectra at room temperature for $Li_{1+x}[(Fe_{1/2}Ni_{1/2})_{0.4}Mn_{0.6}]_{1-x}O_2$ sample series.
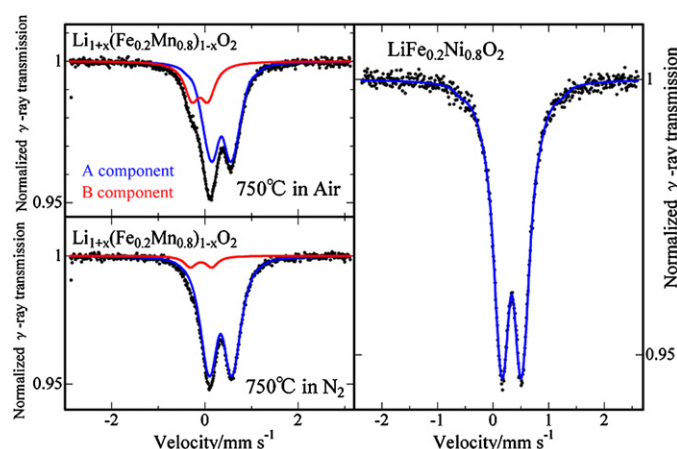

Fig. 15. Observed (closed circle) and calculated (solid curve) ^{57}Fe Mössbauer spectra at room temperature for two $Li_{1+x}(Fe_{0.2}Mn_{0.8})_{1-x}O_2$ samples and $LiFe_{0.2}Ni_{0.8}O_2$.

culated, respectively, as 2.3, 3.0, 2.5, and 2.5 from the peak-top positions of 8.346, 8.349, 8.347, and 8.347 keV. Although no difference in the Ni valence state was observed between 04Y700N and 04Y700A, the Ni ion in 04Y750N was reduced more in the N_2 atmosphere than the Ni ion in 04Y750A. The Ni valence sensitivity is an important factor responsible for the changing x value in $Li_{1+x}(Fe_{y/2}Ni_{y/2}Mn_{1-y})_{1-x}O_2$. The reduced Ni valence close to 2+ state is a valuable strategy for optimizing electrochemical characteristics for the Li_2MnO_3-based positive electrode including Ni.

The ^{57}Fe Mössbauer spectra (Fig. 14) were also sensitive to the calcination condition. The observed spectra for 04Y750N and 04Y700N samples were fitted using only a symmetric doublet with +0.33–0.34 mm s^{-1} of isomer shift (IS) value (Table 5), whereas those for 04Y750A and 04Y700A samples were fitted by two symmetric doublets with different IS values: about +0.3 mm s^{-1} for the A component and 0 mm s^{-1} for the B component. The major component was definitely attributed to high-spin trivalent state of Fe component (IS = +0.33 mm s^{-1}) [19,28]. The minor component was assigned by the tetravalent state of Fe (IS = −0.11 mm s^{-1}) [19,28]. The result represents that the change in the Fe valence state must account for sample calcination, as reported previously for Fe-substituted Li_2MnO_3 because tetravalent Fe existing in the Li–Mn layer of Li_2MnO_3 structure tends to oxidized partially by the presence of adjacent tetravalent Mn^{4+} ion [3,29,30], as is true for Fe ion surrounded by tetravalent Ni ion in $Li_{1-x}NiO_2$ [19]. To examine the Fe valence effect on initial charge and discharge behavior, two $Li_{1+x}(Fe_{0.2}Mn_{0.8})_{1-x}O_2$ samples were prepared using the same calcination temperature (750 °C) and atmosphere (Air or N_2). Their ^{57}Fe Mössbauer spectra (left side in Fig. 15) are rather different from those for 04Y750N and 04Y750A samples, in spite of their adjustment to the same Fe content per chemical formula and preparation conditions. Both $Li_{1+x}(Fe_{0.2}Mn_{0.8})_{1-x}O_2$ samples had higher

amounts of the 4+ state of Fe than those for 04Y750N and 04Y750A samples; moreover, the calcining atmosphere dependence of the valence state of Fe is more remarkable (see Table 5).

The initial charge and discharge curves for $Li/Li_{1+x}(Fe_{0.2}Mn_{0.8})_{1-x}O_2$ cell (Fig. 16) showed that the sample calcined in nitrogen atmosphere had smaller specific capacity greater than 4.4 V to the end of constant-current charging. That fact implies that the formed tetravalent Fe contributes to enhancement of the Li_2O extraction region, as is true also for the tetravalent Mn in Li_2MnO_3. If so, then tetravalent Fe formation must be suppressed. In other words, the Fe valence state should be maintained

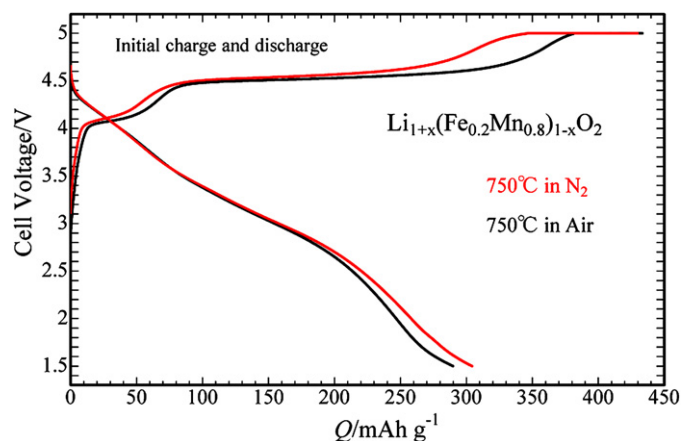Fig. 16. 1st charge and discharge curves for $Li/Li_{1+x}(Fe_{0.2}Mn_{0.8})_{1-x}O_2$ sample cells with two different calcination conditions.

Table 5
^{57}Fe Mössbauer parameters, isomer shift (IS), quadrupole splitting (QS) and line width (Γ) values at room temperature of $Li_{1+x}(Fe_{0.2}Ni_{0.2}Mn_{0.6})_{1-x}O_2$ samples. 20% Fe substituted Li_2MnO_3 or $LiNiO_2$ was used as the standard material.

Sample	A component				B component			
	Fraction (%)	IS (mm s^{-1})	QS[a] (mm s^{-1})	Γ (mm s^{-1})	Fraction (%)	IS (mm s^{-1})	QS (mm s^{-1})	Γ (mm s^{-1})
04Y750A	94.4	+0.3310 (8)	0.43 (3)	0.177 (2)	5.6	−0.046 (12)	0.36 (2)	0.3 (fixed)
04Y750N	100	+0.3342 (4)	0.42 (3)	0.163 (2)	0	–	–	–
04Y700A	96.4	+0.3310 (7)	0.47 (2)	0.162 (4)	3.4	−0.021 (19)	0.42 (3)	0.3 (fixed)
04Y700N	100	+0.3339 (7)	0.43 (3)	0.166 (4)	0	–	–	–
$Li_{1+x}(Fe_{0.2}Mn_{0.8})_{1-x}O_2$ (750 °C in air)	72.1	+0.353 (3)	0.451 (17)	0.220 (5)	27.9	−0.108 (6)	0.348 (11)	0.379 (10)
$Li_{1+x}(Fe_{0.2}Mn_{0.8})_{1-x}O_2$ (750 °C in N_2)	92.4	+0.3364 (17)	0.500 (15)	0.208 (6)	7.6	−0.083 (14)	0.46 (3)	0.31 (3)
$LiFe_{0.2}Ni_{0.8}O_2$ (700 °C in O_2)	100	+0.3353 (7)	0.376 (19)	0.176 (3)	0	–	–	–

[a] Because of the broad nature of the main spectra, the QS distribution from 0 to 2.0 mm s^{-1} was applied to fit them. The average QS values correspond to that at 50% of the cumulative fraction. The error values were derived from gradient and intercept values of least-squares line of the cumulative QS distribution between 30 and 70% of the cumulative fraction.
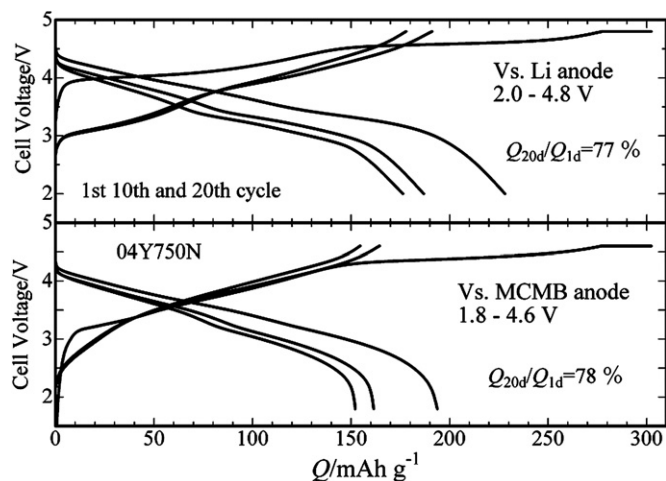
Fig. 17. 1st, 10th, and 20th charge and discharge curves for Li/Li$_{1+x}$[(Fe$_{1/2}$Ni$_{1/2}$)$_{0.4}$Mn$_{0.6}$]$_{1-x}$O$_2$ sample (04Y750N) cell (top panel) and MCMB/Li$_{1+x}$[(Fe$_{1/2}$Ni$_{1/2}$)$_{0.4}$Mn$_{0.6}$]$_{1-x}$O$_2$ sample (04Y750N) cell (bottom panel).

at a trivalent state after incorporating the Li$_2$MnO$_3$ structure. To suppress partial oxidation of trivalent Fe ion, Ni substitution for Fe-substituted Li$_2$MnO$_3$ is believed to be effective because Fe valence in LiNi$_{0.8}$Fe$_{0.2}$O$_2$ is kept at a trivalent state, as shown on the right side of Fig. 15 and Table 5. The Fe valence sensitivity derived from the kind of adjacent transition metal cation should be considered for using the Fe ion in Li$_2$MnO$_3$-based positive electrode material. From the viewpoint of the Fe valence control, Fe- and Ni-substituted Li$_2$MnO$_3$ (Li$_{1+x}$[(Fe$_{1/2}$Ni$_{1/2}$)$_y$Mn$_{1-y}$]$_{1-x}$O$_2$) are evaluated to obtain an appropriate transition metal combination.

Finally, the 04Y750N sample was tested at a full-cell configuration by combining a mesocarbon microbeads (MCMB) anode (Fig. 17). The MCMB/(04Y750N sample) cell was designed in a positive electrode limited configuration. Only the cut-off voltage ranges were changed to 2.0–4.8 V for Li metal and to 1.8–4.6 V for graphite MCMB anodes. Almost identical charge and discharge curves were obtained for Li/04Y750N cell (upper panel in Fig. 17). Initial charge and discharge capacity values were 302 and 228 mAh g^{-1}. At the 20th cycle, the discharge capacity was 176 mAh g^{-1}, which corresponds to 77% against the initial discharge capacity. Although the MCMB/04Y750N cell has smaller initial charge and discharge capacity values (302 and 194 mAh g^{-1}), the discharge capacity at the 20th cycle was 152 mAh g^{-1}, which corresponds to 78% against the initial discharge capacity. We conclude that equal amounts of Fe- and Ni-substituted Li$_2$MnO$_3$ is useful as a positive electrode for a lithium-ion cell, as are other Li$_2$MnO$_3$-based positive electrode materials including Co and Ni [31,32].

4. Conclusion

Equal amounts of Fe- and Ni-substituted Li$_2$MnO$_3$ (Li$_{1+x}$[(Fe$_{1/2}$Ni$_{1/2}$)$_y$Mn$_{1-y}$]$_{1-x}$O$_2$, $0 < x < 1/3$, $0.2 \leq y \leq 0.8$) were synthesized by coprecipitation–hydrothermal–calcination. In contrast to the Fe substituted Li$_2$MnO$_3$, the Fe and Ni substituted Li$_2$MnO$_3$ can act as 3.5 V class positive electrodes with high discharge capacity (>220 mAh g^{-1}), as can other Li$_2$MnO$_3$ positive electrodes, LiNi$_{1/3}$Mn$_{1/3}$Co$_{1/3}$O$_2$–Li$_2$MnO$_3$ if the amount of Fe$_{1/2}$Ni$_{1/2}$ (y) is adjusted to 0.4 or 0.5. Maintaining a single phase of monoclinic Li$_2$MnO$_3$ structure, maximizing the specific surface area and reducing the valence state of Fe and Ni ions must be done with great attention to maintain the attractive electrochemical performance of this material. Especially, minimizing the amount

of tetravalent Fe ion is necessary to reduce Li$_2$O extraction contribution on initial charging. In fact, Ni substitution is effective for that aim. The full-cell test result shows that Fe and Ni substituted Li$_2$MnO$_3$ (Li$_{1+x}$[(Fe$_{1/2}$Ni$_{1/2}$)$_y$Mn$_{1-y}$]$_{1-x}$O$_2$, $0 < x < 1/3$, $0.2 \leq y \leq 0.8$) is attractive as a positive electrode material from the viewpoint of utilization of an inexpensive and plentiful element, Fe, in large-scale lithium-ion batteries.

References

[1] J.B. Goodenough, Y. Kim, Chem. Mater. 22 (2010) 587–603.
[2] B. Ammundsen, J. Paulsen, Adv. Mater. 13 (2001) 943–956.
[3] M. Tabuchi, A. Nakashima, H. Shigemura, K. Ado, H. Kobayashi, H. Sakaebe, H. Kageyama, T. Nakamura, M. Kohzaki, A. Hirano, R. Kanno, J. Electrochem, Soc. 149 (2002) A509–A524.
[4] K. Numata, C. Sasaki, S. Yamanaka, Chem. Lett. (1997) 725–726.
[5] Y.J. Park, Y. Hong, X. Wu, M.G. Kim, K. Ryu, S.H. Chang, J. Electrochem. Soc. 151 (2004) A720–A727.
[6] Z. Lu, D.D. MacNeil, J.R. Dahn, Electrochem. Solid-State Lett. 4 (2001) A191–A194.
[7] C.S. Johnson, J.-S. Kim, C. Lefief, N. Li, J.T. Vaughey, M.M. Thackeray, Electrochem. Commun. 6 (2004) 1085–1091.
[8] M.M. Thackeray, S. Kang, C.S. Johnson, J.T. Vaughey, R. Benedek, S.A. Hackney, J. Mater. Chem. 17 (2007) 3112–3125.
[9] C.S. Johnson, N. Li, C. Lefief, J.T. Vaughey, M.M. Thackeray, Chem. Mater. 20 (2008) 6095–6106.
[10] T.A. Arunkumar, Y. Wu, A. Manthiram, Chem. Mater. 19 (2007) 3067–3073.
[11] A.R. Armstrong, M. Holzapfel, P. Novák, C.S. Johnson, S. Kang, M.M. Thackeray, P.G. Bruce, J. Am. Chem. Soc. 128 (2006) 8694–8698.
[12] F.L. Mantia, F. Rosciano, N. Tran, P. Novák, J. Electrochem. Soc. 156 (2009) A823–A827.
[13] M. Jiang, B. Key, Y.S. Meng, C.P. Grey, Chem. Mater. 21 (2009) 2733–2745.
[14] M. Tabuchi, H. Shigemura, K. Ado, H. Kobayashi, H. Sakaebe, H. Kageyama, R. Kanno, J. Power Sources 97–98 (2001) 415–419.
[15] M. Tabuchi, Y. Nabeshima, M. Shikano, K. Ado, H. Kageyama, K. Tatsumi, J. Electrochem. Soc. 154 (2007) A638–A648.
[16] M. Tabuchi, Y. Nabeshima, K. Ado, M. Shikano, H. Kageyama, K. Tatsumi, J. Power Sources 174 (2007) 554–559.
[17] S. Wu, H. Liu, J. Power Sources 174 (2007) 789–794.
[18] Y. Koyama, I. Tanaka, Y. Kim, S.R. Nishitani, H. Adachi, Jpn. J. Appl. Phys. 38 (1999) 4804–4808.
[19] C. Delmas, G. Prado, A. Rougier, E. Suard, L. Fournès, Solid State Ionics 135 (2000) 71–79.
[20] M. Tabuchi, Y. Nabeshima, T. Takeuchi, K. Tatsumi, J. Imaizumi, Y. Nitta, J. Power Sources 195 (2010) 834–844.
[21] F. Izumi, T. Ikeda, Mater. Sci. Forum 321–324 (2000) 198–203.
[22] P. Strobel, B. Lambert-Andron, J. Solid State Chem. 75 (1988) 90–98.
[23] A. Bommel, J.R. Dahn, Electrochem. Solid-State Lett. 13 (2010) A62–A64.
[24] D. Yu, K. Yanagida, K. Kato, H. Nakamura, J. Electrochem. Soc. 156 (2009) A417–A424.
[25] Z. Lu, Y. Beaulieu, R.A. Donaberger, C.L. Thomas, J.R. Dahn, J. Electrochem. Soc. 149 (2002) A778–A791.
[26] F. Amalraj, D. Kovacheva, M. Talianker, L. Zeiri, J. Grinblat, N. Leifer, G. Goobes, B. Markovsky, D. Aurbach, J. Electrochem. Soc. 157 (2010) A1121–A1130.
[27] J. Kikkawa, T. Akita, M. Tabuchi, M. Shikano, K. Tatsumi, M. Kohyama, J. Appl. Phys. 103 (2008) 104911.
[28] G. Prado, A. Rougier, L. Fournès, C. Delmas, J. Electrochem. Soc. 147 (2000) 2880–2887.
[29] M. Tabuchi, A. Nakashima, K. Ado, H. Kageyama, K. Tatsumi, Chem. Mater. 17 (2005) 4668–4677.
[30] M. Tabuchi, K. Tatsumi, S. Morimoto, S. Nasu, T. Saito, Y. Ikeda, J. Appl. Phys. 104 (2008) 043909.
[31] H. Deng, I. Bellharouak, C.S. Yoon, Y.–K. Sun, K. Amine, J. Electrochem. Soc. 157 (2010) A1035–A1039.
[32] S.-H. Kang, V.G. Pol, I. Bellharouak, M.M. Thackeray, Extended abstract of IMLB2010 (2010) No. 822.